npj Quantum Information

https://doi.org/10.1038/s41534-026-01203-4

Article in Press

Towards telecom-compatible quantum nodes using erbium-doped stoichiometric $EuCl_3 \cdot 6H_2O$ crystals

Received: 10 June 2025

Accepted: 10 February 2026

Cite this article as: Guo, M., Xiao, W., Li, Z. *et al.* Towards telecom-compatible quantum nodes using erbium-doped stoichiometric $EuCl_3 \cdot 6H_2O$ crystals. *npj Quantum Inf* (2026). https://doi.org/10.1038/s41534-026-01203-4

Mucheng Guo, Wanting Xiao, Zongfeng Li, Weiye Sun, Matthew J. Sellars, Rose L. Ahlefeldt, Ping Wang, Shuping Liu, Fudong Wang & Manjin Zhong

1,2]Mucheng Guo 1]Wanting Xiao 1,5]Zongfeng Li 1,2]Weiye Sun 3]Matthew J. Sellars 3]Rose L. Ahlefeldt 4]Ping Wang 2]Shuping Liu liushuping@iqasz.cn 2]Fudong Wang fdwang.phys@foxmail.com 2]Manjin Zhong manjin.zhong@gmail.com
[1]Southern University of Science and Technology, Shenzhen 518055, China
[2]International Quantum Academy, and Shenzhen Branch, Hefei National Laboratory, Shenzhen 518048, China
[3]Centre of Excellence for Quantum Computation and Communication Technology, Research School of Physics, Australian National University, Canberra, ACT 0200, Australia
[4]Faculty of Arts and Sciences, Beijing Normal University, Zhuhai 519087, China
[5]Present affiliation: Department of Electrical and Computer Engineering and Applied Physics Program, Northwestern University, Evanston, IL 60208, USA

Abstract

Doping erbium ions into europium-based hosts offers a promising platform for quantum repeater nodes, combining europium's exceptional coherence properties for long-term quantum storage with erbium's microwave compatibility and direct telecom-band emission for efficient optical interfacing. In this work, we investigated erbium-doped $EuCl_3 \cdot 6H_2O$ stoichiometric crystals as a candidate for such nodes. We demonstrate that erbium doping shifts the optical transition frequencies of nearby Eu^{3+} ions, producing well resolved satellite lines in the inhomogeneous absorption profile. We experimentally probe the coupling between Er^{3+} and Eu^{3+} ions under varying temperature and magnetic field conditions, quantifying the interaction strength, which ranges from tens to hundreds of kilohertz, depending on field orientation, magnitude, and the lattice position of the Eu^{3+} ions. At 60 mK and a moderate magnetic field of 0.1 T, we observed a strong frozen core effect from Er^{3+} spins, substantially extending the Eu^{3+} optical coherence time from 62 μs to 162 μs, approaching the lifetime limit, and enabling hour-long hyperfine state lifetimes. These results underscore the potential of dual-species rare-earth systems for photonic quantum technologies and highlight their promise for precise quantum control.

Towards Telecom-Compatible Quantum Nodes Using Erbium-Doped Stoichiometric $\mathbf{EuCl_3 \cdot 6H_2O}$ Crystals

[

February 12, 2026

1 Introduction

The realization of large-scale quantum networks depends critically on the development of high-fidelity quantum nodes that combine efficient optical interfaces with long-lived quantum memories (1; 2; 3). Rare-earth-ion-doped crystals have emerged as a promising material platform for this purpose, particularly in applications that require multiple stationary qubits with long coherence times and direct compatibility with telecom-wavelength photons (4; 5). Within this class of materials, europium (Eu^{3+}) and erbium (Er^{3+}) ions stand out for their unique and complementary properties: Eu^{3+} offers exceptional optical and spin coherence times, making it an excellent candidate for quantum storage and processing (6; 7; 8; 9), while Er^{3+} features optical transitions in the telecom C-band (∼1.5 m), enabling seamless integration with fiber-optic communication infrastructure (10; 11; 12; 13; 14).

In this context, stoichiometric europium crystals present a compelling platform in which Er^{3+} ions can be intentionally introduced as active qubits that interact with the densely packed Eu^{3+} ions naturally present in the host lattice (15). This architecture enables a novel hybrid quantum node design: Er^{3+} ions serve as tunable optical interfaces and mediators of interaction, while Eu^{3+} ions act as long-lived quantum memories (Figure 1) (16). Moreover, the large and anisotropic electronic spin of Er^{3+} in low-symmetry environments allows for controllable dipolar interactions with neighboring Eu^{3+} ions, creating an addressable spin ensemble capable of supporting multi-qubit quantum registers (17).

However, the incorporation of Er^{3+} ions inevitably perturbs the local Eu^{3+} environment through lattice strain and electric and magnetic dipolar fields. Understanding these Eu–Er coupling mechanisms is essential for elucidating the microscopic behavior of this hybrid rare-earth system and optimizing it for quantum repeater node applications. Moreover, while stoichiometric crystals offer well-defined Eu^{3+} ion positions and a highly ordered crystal field, their

Figure 1: **Telecom-band quantum node based on Er^{3+} ion doped stoichiometric europium crystals.** a) Schematic of a telecom-band quantum node using Er^{3+} ion doped stoichiometric europium crystals, where Er^{3+} ions serve as the quantum interface operating at telecommunication wavelengths, while nearby Eu^{3+} ions act as long-lived quantum memories. b) The schematic energy level diagram of the Er^{3+} and Eu^{3+}ions with δf denotes the static optical frequency shift arising from the size mismatch between Er^{3+} and Eu^{3+} ions.

high rare-earth-ion density raises concerns about interaction-induced decoherence, which must be carefully managed.

Here, we investigate the stoichiometric crystal $EuCl_3 \cdot 6H_2O$, chosen for its long coherence times and exceptionally narrow inhomogeneous linewidths (100 MHz) that enable high-precision quantum control (15). Doping with 0.1% Er^{3+} realizes a hybrid Eu–Er system bridging Eu-based quantum memories with telecom-band optical transitions. Using satellite-line spectroscopy, we map local Eu–Er configurations and quantify frequency shifts and broadening mechanisms. Temperature- and field-dependent photon-echo measurements reveal how Er-induced local fields influence Eu^{3+} coherence and elucidate the Eu–Er coupling. Eu^{3+} ions near Er^{3+} exhibit pronounced frequency shifts, producing well-resolved satellite lines. Above 2 K, Er^{3+} significantly shortens the optical coherence of nearby Eu^{3+} ions, while below 2 K this effect becomes insignificant. Under magnetic fields, the Er-induced effects are strongly anisotropic and at field intensity above 1 T, frozen Er^{3+} electronic spins significantly suppress Eu–Eu interactions. These findings establish this hybrid rare-earth platform as a promising testbed for efficient, telecom-compatible quantum repeater nodes (16)

2 Results

2.1 Resolving Eu^{3+} Sites Proximal to Er^{3+} Dopant

The $EuCl_3 \cdot 6H_2O$ crystal has a monoclinic structure and belongs to the P2/n space group (No.13), with the single Eu^{3+} site exhibiting C_2 symmetry. In this study, both undoped $EuCl_3 \cdot 6H_2O$ crystals and 0.1% Er^{3+} doped $EuCl_3 \cdot 6H_2O$ crystals were grown from an aqueous solution at near room temperatures as detailed in reference (15). These crystals have the smallest dimension along the [010] (C_2) axis and a single cleavage plane along the [100] direction. For spectroscopy and coherence time measurements, the crystal was cleaved along the (100) plane, and the sample had a thickness of approximately 2 mm along the light propagation direction ([100] axis). The laser was linearly polarized along the [010] axis to maximize absorption. The orientation of the crystal and the experimental setup is illustrated in the methods section and Supplementary Figure 1.

We performed spectroscopic measurements of the $^7F_0 \rightarrow {}^5D_0$ transition of

Figure 2: **Excitation spectrum of the $^7F_0 \rightarrow {}^5D_0$ transition for Eu^{3+} ions in the 0.1%Er^{3+} : $EuCl_3 \cdot 6H_2O$ crystal (red) and the undoped $EuCl_3 \cdot 6H_2O$ crystal (black)**. The satellite lines are labeled as peaks A, B, and C from left to right. The frequency spot at the main peak (-2.9 GHz) abelled as D was involved in some measurements.

Figure 3: **Two pulse photon echo measurements and optical coherence of Eu^{3+} satellite lines in Er^{3+} : $EuCl_3 \cdot 6H_2O$**. a) The top subplot shows the the two-pulse photon echo (TPPE) amplitude for the Eu^{3+} satellite lines of the Er-doped crystal with a fixed delay of $\tau = 10$ s, while another laser was tuned to scan through the $^4I_{15/2} \rightarrow {}^4 I_{13/2}$ transition of the Er^{3+} ions as shown in the bottom subplot. b) The TPPE decay curves of Eu^{3+} satellite lines in the Er-doped crystal and in the undoped crystal recorded at a temperature of approximately 60 mK. The solid lines represent the fitting resulted from the single-exponential model $A(\tau) = A_0 \exp[(-\frac{2\tau}{T_2})]$, where A_0 is the initial echo amplitude, and 2τ represents the total delay between the first $\pi/2$ pulse and the echo. The fitting resulted optical T_2 values of 62.8 ± 3.6 s, 55.3 ± 3.9 s and 43.6 ± 2.1 s for the three satellite lines respectively and of 79.4 ± 3.7 s for the undoped sample. c) Temperature dependence optical homogeneous linewidth Γ_h of Eu^{3+} satellite lines. The solid lines for satellite lines B and D show the fitting results from a phenomenological formula $\Gamma_h(T) = \Gamma_0 + \Gamma_{SD} e^{\frac{-(T-T_{SD})^2}{2\sigma^2}} + \alpha_{phonon} T^7$, where the Gaussian function is used to capture the feature of the bump peak Γ_{SD} near 2.9 K and α_{phonon} presents the line broadening contributed by the two-phonon Raman process. The dashed lines for lines A and C are shown only as guides to the eye, as the data above 3 K are too limited to reliably extract the fit parameter. All measurements were performed in the absence of an external magnetic field.

Eu^{3+} to examine changes in transition frequencies and inhomogeneous broadening induced by Er^{3+} doping. To enable analysis of Eu-Er interactions in subsequent experiments, we also measured the Er^{3+} spectra, focusing on the magnetic-field dependence of their optical transition frequencies, from which we extracted the g-factors. Due to the strong absorption of the dense Eu^{3+} ions in this material, direct transmission (absorption) measurements would be severely saturated. The inhomogeneous lineshape of the Eu^{3+} ions, recorded as an excitation spectrum in both the Er-doped crystal and the undoped crystals, is shown in Figure 2. These measurements were conducted at a temperature of 60 mK and in the absence of an external magnetic field. The Er-doped crystal exhibits a broad primary excitation feature centered around $\sim$ 517148.5 GHz (579.7028 nm in vacuum), which is significantly broader compared to the undoped crystal. Additionally, the Er-doped crystal shows three distinct satellite lines, labeled as A (-8.5 GHz), B (+5.0 GHz), and C (+6.9 GHz), which arise due to local strain caused by the ionic radius mismatch between Er^{3+} and Eu^{3+} (18). Thus, each satellite line relates to the ensemble of Eu^{3+} ions occupying

a particular position adjacent to the dopant Er^{3+} ion. Based on prior studies (18; 19), we assign the crystallographic sites of these peaks by examining their frequency shifts and their distance from the Er^{3+} dopant, as summarized in Supplementary Table 1. Specifically, peak C corresponds to ions located at one of two possible crystallographic sites along the C_2 axis, while peak A and B are associated with ion sites off the C_2 axis. The linewidths of these satellite lines are comparable to those observed in the undoped crystal, suggesting that the doping of Er^{3+} does not significantly contribute to line broadening of the Eu^{3+} transition. This observation supports the interpretation that the broadening of the central peak for Er-doped crystal is primarily due to a large number of poorly resolved satellite lines.

For the Er^{3+} ions, measurement of the electronic Zeeman g-factor was realized by performing optical spectroscopy of the $^4I_{15/2} \rightarrow {}^4I_{13/2}$ ($Z_1 \rightarrow Y_1$) transition at 60 mK with an external magnetic field applied (detailed in Supplementary information). Along the C_2 axis, the measured g-factor are $= 0.70 \pm 0.04$ for the ground state (Z_1) and $_e = 0.12 \pm 0.04$ for the excited state (Y_1) (Supplementary Figure S2a). In the plane perpendicular to the C_2 axis, the g-factor values exhibits strong anisotropy , with a maximum exceeding 13 and a minimum approaching zero (Supplementary Figure S2c), closely matched those obtained from EPR measurements in the Er^{3+} doped $YCl_3 \cdot 6H_2O$ crystal (20).

2.2 Interactions between Eu^{3+} and Er^{3+} in the absence of a magnetic field

We explored the potential to indirectly manipulate nearby Eu^{3+} via the dopant Er^{3+} by using a laser to intentionally perturb the Er^{3+} ions optically prior to the two-pulse photon echo (TPPE) sequence on the Eu^{3+} ions. The results is present in Figure 3a, with the pulse sequences applied shown in the inset.

The scrambler laser frequency of the Er^{3+} scanned through 1533.9 nm ($Z_1 \rightarrow Y_1$ transition), while the echo amplitude of Eu^{3+}, at a fixed delay of τ=10 s, was monitored. When the scrambler laser beam is resonant with the $Z_1 \rightarrow Y_1$ transition, optical excitation of Er^{3+} ions changes their electric dipole moments, which in turn alters the local electric field experienced by the nearby Eu^{3+} ions (21; 22; 23). This perturbation induces small shifts in the Eu^{3+} optical transition frequencies, leading to decoherence, as evidenced in Figure 3a by the significantly decreased echo amplitude across all satellite lines. Notably, satellite line A and C exhibit greater reductions than line B, indicating that the corresponding Eu^{3+} sites are strongly coupled to Er^{3+} ions, whereas those Eu^{3+} ions associated with line B experience weaker coupling.

Next, the optical coherence time of Eu^{3+} at each satellite line was measured without applying an intentionally perturbing laser on the Er^{3+} ions. For comparison, the coherence time of Eu^{3+} in an undoped crystal was also measured. The TPPE decays of these measurements are presented in Figure 3b. The echo envelope attenuation for all datasets exhibits an exponential form and can be well described by a standard relaxation time T_2. Fitting the data yields the optical homogeneous linewidth Γ_h, which are related to the coherence time T_2

Figure 4: **Stimulated photon echo decay of Eu^{3+} satellite lines.** a-c) The measured stimulated photon echo (SPE) decay of the Eu^{3+} as a function of the separation T_w for satellites A, B, and C in the Er-doped crystal, with a fixed time $\tau = 7$ μs. The inset presents the Fast Fourier transform results, modulated from the SPE for different T_w ranges, which was processed by removing the DC component through subtraction of the double-exponential fitting results. All measurements were performed in the absence of an external magnetic field.

by $\Gamma_h = 1/\pi T_2$, as 5.1 ± 0.3 kHz, 5.7 ± 0.4 kHz, 7.3 ± 0.4 kHz for Eu^{3+} ions corresponding to satellite line peaks A, B, and C, respectively.

These values are only slightly broader than that of the undoped crystal (Γ_h=4.0 $\pm$0.2 kHz), indicating limited decoherence effects of Er^{3+} dopants on the nearby Eu^{3+} ions. This can be attributed to the low temperature (at approximately 60 mK) we used during the measurements, when electronic spin flips of Er^{3+} are largely suppressed.

We extended the coherence time measurements of Eu^{3+} at the three satellite lines and the undoped crystal to a broader temperature range, from 60 mK to 10 K. In addition, the measurements were also performed at a frequency detuned by approximately -2.9 GHz within the primary spectral feature of the Er-doped crystal, labelled as 'D' in Figure 2. As shown in Figure 3c, the homogeneous broadening of the undoped crystal saturates at temperatures below 4 K, and exhibits a T^7 dependence at higher temperatures (24; 25). This behavior suggests that the optical decoherence of Eu^{3+} in the undoped crystal is primarily governed by two-phonon Raman processes.

For the Er-doped crystal, all four Eu^{3+} groups (A, B, C, and D) exhibit similar saturation behavior in the Γ_h below 2 K at a level comparable to that observed in the undoped crystal. Above 2 K, however, Γ_h increases more rapidly with temperature across all satellite lines and the D point. Notably, satellite peaks A and C show a more pronounced increase, likely due to their stronger coupling with the Er^{3+} ion, compared to satellite B and the D point. This steepening is attributed to the rapid increase in the electronic spin relaxation rate of Er^{3+} above 2 K.

Additionally, both satellite B and the D point display a distinct bump near 2.9 K, which we attribute to a narrowing effect analogous to motional narrowing (26). As temperature rises, the spin relaxation rate becomes significantly larger than the interaction strength induced in nearby Eu^{3+} ions (group B and D). In this regime, the fluctuations from Er^{3+} spin flips are averaged out over the measurement window, leading to a reduction in Eu^{3+} homogeneous broadening. In contrast, satellite lines A and C, which couple more strongly to Er^{3+}, are expected to exhibit such narrowing peaks at higher temperatures that fall outside our measurement range (discussed in more detail later). Above 6 K, homogeneous broadening is again dominated by two-phonon Raman processes ($\Gamma_h \propto T^7$), as previously discussed and consistent with other Eu^{3+}-doped systems (25; 24).

To further quantitatively investigate the Eu–Er interactions, we employed the stimulated photon echo (SPE) technique using a $\pi/2-\tau-\pi/2-T_w-\pi/2-\tau$ sequence. Compared with TPPE, SPE offers an extended measurement time window, enabling higher precision in frequency determination (27; 28). The SPE decay curves of Eu^{3+} ions in satellite lines A, B, and C at 60 mK are shown in Figure 4(a-c). Exponential decay fits yield excited-state lifetimes of 89.0 s, 96.9 s and 54.3 s, respectively, consistent with luminescence decay measurements for these sites (Supplementary Table S1). Clear modulations appear in the echo envelopes, indicating frequency shifts in Eu^{3+} ions due to coupling with the Er^{3+}. Fast Fourier Transform (FFT) analysis (Figure 4 (a-c), insets) reveals two frequency components per curve, with the higher-frequency component vanishing for $T_w \gg 200$ s. We thus attribute the higher-frequency component to interactions involving the excited state ($^5D_0$) of Eu^{3+} and the lower-frequency component to interactions involving the ground state ($^7F_0$). These results, summarized in Supplementary Table S1 , agree with calculations based on magnetic dipole–dipole interaction models.

Table 1: Calculated (magnetic dipole–dipole model) and experimental results (SPE) for variation in transition frequencies for Eu^{3+} at the satellite lines due to magnetic dipole–dipole interactions with the Er^{3+}. $|\delta^{g}_{\omega}|$ and $|\delta^{e}_{\omega}|$ represent the fluctuation amplitudes of the Eu^{3+} transition frequency caused by nearby Er^{3+} ions, corresponding to the ground and excited states, respectively. The details of the calculation are presented in Methods.

line ions	calculated		
$\lvert\delta^{g}_{\omega}\rvert$ (kHz)	SPE		
$\lvert\delta^{g}_{\omega}\rvert$ (kHz)	SPE		
$\lvert\delta^{e}_{\omega}\rvert$ (kHz)			
A	100.7	101.9	230.5
B	23.9	16.4	39.0
C	93.3	58.0	92.6

To quantify the decoherence induced by Er^{3+} ions, we model the process as a Gauss-Markov stochastic modulation. In this framework, the TPPE decay of Eu^{3+} is given by (29; 30):

$$L_G(t) = \mathrm{Exp}\{-\frac{\delta_{\mathrm{w}}^2}{{R_{Er}}^2}[R_{Er}t - 3 + 4\mathrm{e}^{-R_{Er}t/2} - \mathrm{e}^{-R_{Er}t}]\} \quad (1)$$

Here, δ_w characterizes the fluctuation amplitude of the Eu^{3+} transition frequency caused by Er^{3+}, and R_{Er} is the Er^{3+} electronic spin relaxation rate.

Figure 5: **Calculated Er^{3+} spin relaxation and predicted Eu^{3+} linewidth broadening.** a) The calculated Er^{3+} electron spin relaxation rate R_{Er} from Equation 2. The inset shows a rapid increase in R_{Er} starting from 2 K, reflecting enhanced relaxation processes. The labelled 2.9 K is where we observed bump in the broadening for satellite line B and D point shown in Figure 3. The red crosses represent R_{Er} values along satellite line B at 2 K and 2.9 K, corresponding to the initial increase and saturation of the homogeneous linewidth. b) Predicted temperature dependence broadening for the satellite line Eu^{3+} ions, calculated using the diffusion model of Equation 1.

The values of δ_ω used for calculation are the $\delta_\omega^{\mathrm{g}}$ values taken from the SPE measurements listed in Table 1.

We assume that R_{Er} is governed by the Orbach process (20), described by :

$$R_{Er} = \alpha_{\mathrm{o}} \mathrm{e}^{-\Delta/T} \tag{2}$$

where $\Delta = 24.5$ K (16.8 cm^{-1}) corresponds to the energy of the Z_2 excited state (31), and α_o is the Orbach coefficient. Substituting Equation 2 into Equation 1 and solving for $L_G(t = \mathrm{T}_2) = \mathrm{e}^{-1}$ yields the temperature-dependent homogeneous broadening of the Eu^{3+} satellite lines, parameterized by α_o.

Based on the experimentally observed peak at 2.9 K for satellite line B (Figure 3c), we estimate $\alpha_o \approx 9 \times 10^4$ kHz. This value is approximately an order of magnitude higher than that derived from EPR measurements of Er^{3+} in $YCl_3 \cdot 6H_2O$ (20), likely due to the presence of an applied magnetic field in the latter experiment. Using Equation 2, we calculate R_{Er} as a function of temperature (Figure 5a).

The resulting temperature-dependent homogeneous linewidths for the Eu^{3+} satellite lines, derived from the model, are shown in Figure 5b. Compared to satellite line B, satellite lines A and C, the narrowing peaks occurs at higher temperatures (3.7 K and 3.4 K, respectively), consistent with their stronger coupling to Er^{3+}. Likewise, the peak Γ_{h} values for A and C are higher than that of B.

However, certain features in the experimental data (Figure 3c) are not fully captured by our simulations. For instance, in satellite line B, (i) the homogeneous linewidth shows a sharp resurgence following the narrowing peak, and (ii) the peak value of Γ_{h} is significantly higher than predicted. We hypothesize that these discrepancies may stem from several factors. First, lattice distortions arising from the ionic radius mismatch of Er^{3+} may enhance phonon-mediated decoherence at relatively low temperatures. Second, the presence of multiple Er^{3+} isotopes and their complex hyperfine structures may contribute additional decoherence channels for nearby Eu^{3+} ions—effects not fully accounted for in our model.

Figure 6: **Magnetic field dependence of optical coherence in Eu^{3+} ions.** a) The optical Γ_h of the Eu^{3+} at the satellite lines (top) and the g-factor value of Er^{3+} (, bottom) as a function of the magnetic field orientation in the plane perpendicular to the C_2 axis, with a fixed field strength of $|\mathbf{B}| = 0.1$ T. b) The TPPE decays of the Eu^{3+} at the satellite lines, measured at $\theta = 100°$($|\mathbf{B}| = 0.1$ T). An exponential fitting resulting optical coherence time of 161.8 ± 9.3 s, 155.7 ± 10.1 s, and 85.3 ± 4.2 s for satellite lines A, B, and C, respectively. A free running laser, without frequency stabilization, was used for these measurements to minimize phase noise during feedback correlation. c) The optical Γ_h of Eu^{3+} as a function of the magnetic field strength applied along θ=100° in the plane perpendicular to the C_2 axis. The inset shows an expanded view for $|\mathbf{B}| \leq 0.1$ T. (d) The optical Γ_h of Eu^{3+} as a function of the magnetic field strength applied along the C_2 axis. The solid lines in (a), (c) and d) are merely connecting lines between data points.

2.3 Magnetic field effects on Er^{3+} and Eu^{3+} dynamics

In this section, we investigated how variations in the orientation and magnitude of the magnetic field affect the dynamics of Er^{3+} ions and, in turn, influence nearby Eu^{3+} ions. Our primary objectives are to characterize the $Eu - Er$ coupling and to identify magnetic field conditions that optimize the optical coherence time of the satellite-line Eu^{3+} ions.

As in the g-factor measurements (Supplementary Figure 2), we applied a moderate magnetic field of $|\mathbf{B}| = 0.1$ T at a fixed temperature of 60 mK and measured the optical linewidth Γ_h of Eu^{3+} ions as the magnetic field was rotated in the plane perpendicular to the C_2 axis (Figure 6a).

In the undoped crystal, the optical linewidth Γ_h exhibited no dependence on the rotation angle θ, as expected. In contrast, in the Er-doped crystal, Γ_h for all Eu^{3+} satellite lines displayed a clear periodic angular dependence. Local minima of Γ_h occurred at $\theta \sim 10°$ and 190°, coinciding with -factor minima of Er^{3+} spins (Figure 6a). Interestingly, the global minima of Γ_h for all satellite lines, appeared at $\theta \sim 100°$ (and 280°), where the Er^{3+} -factor reaches its maximum. At this magnetic field orientation, the optical coherence times of Eu^{3+} ions were measured to be 161.8 ± 9.3 s, 155.7 ± 10.1 s, and 85.3 ± 4.2 s for satellite lines A, B, and C, respectively - approaching their state-lifetime limits (Figure 6b).

This reflects the role of angular dependent g-factor value of the Er^{3+} spins in modulating the coherence properties of nearby Eu^{3+} ions (more direct image in Supplementary Figure S4). When the -factor () is small, the Er^{3+} spin flips cause minimal field perturbation to nearby Eu^{3+}. As the -factor increases, both the interaction strength (δ_ω^g) and the rate (R_{Er}) of magnetic field perturbations increase (20), resulting in linewidth broadening in all satellite line Eu^{3+} ions. At even larger -factor, when the Zeeman splitting of Er^{3+} spin levels become significant, compared to kT, the lack of available phonon density cause the electron spin been frozen into the lower spin state. This also suppress the flip-

flop process because there is limited ions in the upper spin state for exchanging energy with that in the lower state. The resulted spin 'freezing' (lower R_{Er}) of Er^{3+} induces frozen core effect on the nearby Eu^{3+} and thus narrowing Γ_h (32).

We further examined linewidth behavior under increasing magnetic field strength applied along two directions: the C_2 axis (g-factor minimum ~0.7) and $\theta = 100°$ (g-factor maximum ~13.46). For each orientation, we measured Eu^{3+} optical homogeneous linewidths at satellite lines A, B, C and the undoped crystal.

In the undoped crystal (Figure 6cd), the homogeneous broadening steadily increased with field strength for both orientations, saturating at 2.5 T along the C_2 axis. This behavior arises from the quadratic Zeeman effect, where an applied magnetic field induces a moment in Eu^{3+} ions, enhancing their dipole-dipole interactions with each other and broadening the linewidth. At higher fields, a large energy gap of Eu^{3+} is created through Zeeman effect, resulting in frozen core effect which suppress the dipole-dipole interaction between these Eu^{3+} ions, leading to saturation and a slight narrowing.

In the Er-doped crystal, a distinct trend emerged across both orientations: as field strength increased, Eu^{3+} linewidths became narrower than in the undoped sample. We attribute this to the frozen core effect induced by Er^{3+} spins. Here, two key points merit attention: (1) Er^{3+} spins must be frozen before they can stabilize nearby Eu^{3+} spins; (2) as field increase, Eu^{3+} ions experience both frozen core stabilization from Er^{3+} and dipole-dipole interactions with other Eu^{3+} ions.

Although quantitatively modeling this influence is difficult, we can infer trends by comparing Er-doped and undoped results. Along the $\theta = 100°$ direction (Figure 6c), all satellite lines initially exhibit narrowing with increasing field and reach minimum linewidths around 0.01 T. Beyond this, A and C saturate, while B gradually broadens. This suggests that Er^{3+} spins are effectively frozen above 0.01 T, maximizing the stabilization of Eu^{3+} at A and C. In contrast, the Eu^{3+} at satellite line B, which couples more weakly to Er^{3+}, continues to broaden due to residual Eu–Eu dipole interactions, resembling the undoped case.

Along the C_2 axis (Figure 6d), although all satellite lines show increasing linewidths with field, the rate is slower than in the undoped sample. Around 0.2 T, the linewidths fall below those of the undoped crystal, implying that Er^{3+} spins are frozen. However, due to the small g-factor, the coupling of all satellite line Eu^{3+} to Er^{3+} remains weak, and dipole interactions among Eu^{3+} dominate. As a result, the Eu^{3+} satellite lines continue to broaden and eventually saturate—again mirroring the undoped case. Importantly, the magnetic field required to freeze Er^{3+} spins differs by a factor of 20 between the two directions (0.01 T and 0.2 T)—roughly an inverse match to the ratio of their g-factors, consistent with expectations.

Finally, we explored the impact of Er^{3+} spin freezing on Eu^{3+} hyperfine dynamics. At $\theta = 100°$ and $|\mathbf{B}| = 0.1$ T, where the g-factor of Er^{3+} is maximized and the frozen core effect is most pronounced, the Eu^{3+} hyperfine lifetime (T_1^s) measured via spectral hole burning exceeded its zero-field value by over three

orders of magnitude (see Supplementary information). The longest T_1^s was observed for satellite line A, reaching 4200 s (over 1 hour), suggesting hyperfine coherence time up-limit of 2 hours.

3 Discussion

In this study, we conducted satellite line spectroscopy and photon echo measurements on a 0.1% $Er^{3+} : EuCl_3 \cdot 6H_2O$ crystal to assess the potential of this system for developing quantum repeater nodes. We characterized the coupling between Er^{3+} dopants and nearby Eu^{3+} ions, revealing well-resolved frequency satellite lines in the Eu^{3+} inhomogeneous profile, attributed to ionic radius mismatch. At sub-Kelvin temperatures, both inhomogeneous and homogeneous optical linewidths of these satellite lines were comparable to those in undoped $EuCl_3 \cdot 6H_2O$ crystals.

Upon optical excitation of Er^{3+}, we observed echo demolition effects. Even without deliberately driving Er^{3+} transitions, temperature-dependent decoherence in neighboring Eu^{3+} ions was detected, driven by Er^{3+} spin dynamics. Stimulated photon-echo modulation measurements quantified the Eu^{3+}–Er^{3+} coupling, which follows a dipole–dipole interaction model. We measured effective coupling strengths of approximately 100 kHz for nearest-neighbor Eu–Er pairs. This coupling magnitude is central to enabling coherent quantum-state transfer: if Er^{3+} coherence can be extended to the sub-millisecond regime, coherent swap or controlled-phase operations between telecom-band Er^{3+} qubits and storage-efficient Eu^{3+} ensembles become feasible using advanced dynamical control protocols such as PulPol and ZenPol (33; 34; 35).

Under a 0.1 T magnetic field, we achieved an optical coherence time of 162 s and a hyperfine-state lifetime exceeding one hour, demonstrating the promise of Eu^{3+} for long-lived quantum storage. Further improvements can be realized by deuterating the crystal to suppress nonradiative decay through O–H vibrations (15; 36). By deuterating the crystal, it is also possible to extend both the optical and spin coherence times of Er^{3+} ions. When complemented by reduced Er^{3+} doping concentration and Er^{3+} electronic spin polarization under low temperatures and high magnetic fields, this approach is highly promising for attaining the coherence time of Er^{3+} necessary for building quantum nodes.

The Er^{3+} concentration, however, introduces an inherent trade-off in designing such hybrid quantum systems. Increasing Er^{3+} content enhances the optical depth of the Eu^{3+} satellite transitions, beneficial for spectral tailoring and multiplexed memory protocols. However, it also amplifies lattice strain and both Er–Er and Eu–Er dipolar interactions, leading to additional spectral broadening and accelerated decoherence for both Er^{3+} and Eu^{3+}. Optimizing this balance—between optical depth, spectral purity, and coherence time—will be essential for developing robust and scalable telecom-compatible quantum repeater nodes based on stoichiometric rare-earth crystals.

Analyzing the decoherence dynamics of central ions influenced by the surrounding spin bath is a significant focus in quantum systems based on solid-

stated defects. In most cases, the dynamics of the spin bath is indirectly analyzed by observing the central ion. However, in the current system, Eu^{3+} ions serve as a spin bath for Er^{3+} ions. By directly optically driving these environmental ions, we observed and analyzed the dynamic process related to the central spin, such as the 'frozen core' effect. This work complements existing theoretical and experimental framework in solid-state quantum systems.

Methods

Experimental setup

With the experimental setup, as depicted in Supplementary Figure 1a, the crystal was mounted on a copper sample holder and enclosed in a sealed glass container filled with nitrogen gas to prevent efflorescence of the sample in vacuum. This setup was mounted inside a dilution fridge (LD400, Bluefors), maintaining a base temperature of approximately 60 mK. A three-dimensional vector superconducting magnet (American Magnetics Inc.) was employed to generate an external magnetic field, with field strength up to $|\mathbf{B}| = 5$ T along the [010] (C_2) axis and $|\mathbf{B}| = 1$ T in the (010) plane, as depicted in Supplementary Figure 1b.

The $^7F_0 \rightarrow {}^5D_0$ optical transition for Eu^{3+} ions, excited around 580 nm, and the $^4I_{15/2} \rightarrow {}^4I_{13/2}$ transition for Er^{3+} ions, excited around 1534 nm, were driven by two separate diode lasers from Toptica. The 580 nm laser has a linewidth of approximately 10 kHz, with its frequency stabilized using a commercial metrological-grade Fabry-Perot cavity (Stable Laser Systems). The frequency and intensity for both laser beams were modulated using acousto-optic modulators (AOM1 and AOM2).

Photon echo measurement

Two pulse photon echo measurements on the $^7F_0 \rightarrow {}^5D_0$ optical transition of Eu^{3+} ions were performed using $\pi/2$ pulses of 1 μs and π pulses of 2 μs, generated via an acousto-optic modulator (AOM1). For stimulated photon echo measurements, three pulses of 1 μs duration were applied. The echo amplitude was detected by interfering it with a local oscillator frequency-shifted by approximately 21 MHz, and the resulting beat signal was recorded using a photodetector.

Eu^{3+}- Er^{3+} interaction of different satellite lines

The decoherence of Eu^{3+} ions located near Er^{3+} dopants is primarily governed by magnetic dipole–dipole interactions between the two species (37). For a Eu^{3+} ion at a relative position $\boldsymbol{r}$ with respect to a neighboring Er^{3+} ion, the interaction Hamiltonian takes the standard form:

$$H_{dd} = \frac{\mu_0}{4\pi}\left[\frac{\boldsymbol{\gamma}_{Eu}\cdot\boldsymbol{\gamma}_{Er}}{|\boldsymbol{r}|^3} - \frac{(\boldsymbol{\gamma}_{Eu}\cdot\boldsymbol{r})(\boldsymbol{\gamma}_{Er}\cdot\boldsymbol{r})}{|\boldsymbol{r}|^5}\right], \tag{3}$$

where $\boldsymbol{\gamma}_{Eu}$ and $\boldsymbol{\gamma}_{Er}$ are the gyromagnetic ratios of Eu^{3+} and Er^{3+}, respectively. This interaction may lift the effective C_2 symmetry between otherwise crystallographically equivalent Eu^{3+} sites.

However, $\boldsymbol{\gamma}_{\mathrm{Er}}$ is not well-defined in the absence of an external magnetic field, and the complex hyperfine structure of Eu^{3+} complicates accurate modeling of the dipole–dipole interaction. To estimate the interaction strength in the $^7F_0$ ground state, we approximated the decoherence-inducing energy shift as:

$$\delta_\omega^g = \frac{\mu_0}{4\pi} \frac{\boldsymbol{\gamma}_{Eu} \boldsymbol{\gamma}_{Er}}{|\boldsymbol{r}|^3} \tag{4}$$

where anisotropy in the magnetic moment was neglected, and both gyromagnetic ratios were taken as effective scalar values: $\gamma_{\mathrm{Eu}} \approx 2$ MHz/T and $\gamma_{\mathrm{Er}} \approx 98$ GHz/T (half of the maximum). Hyperfine-level contributions were also disregarded in this approximation.

Data availability

The data for the current study are available via Zenodo (https://zenodo.org/records/18229971). No other publicly available datasets or sequences were used in this study.

Code availability

All data and figures are original and generated by the authors using appropriate licensed software. Scripts and routines used to produce these figures are available from the corresponding author upon reasonable request.

Acknowledgments

This work was supported by the Quantum Science and Technology-National Science and Technology Major Project (No. 2021ZD0301204), the National Natural Science Foundation of China (Grant No. 11904159, 12004168 and 12304454), Guandong Innovative and Entrepreneurial Research Team Program (Grant No. 2019ZT08X324), Guangdong Basic and Applied Basic Research Foundation (Grant No. 2021A1515110191), and the Key-Area Research and Development Program of Guangdong Province (Grant No. 2018B030326001), the Science, Technology and Innovation Commission of Shenzhen Municipality (KQTD20210811090049034).

Author Contributions

F. Wang, R. Ahlefeldt, M. Sellars and M. Zhong conceived the project. W. Xiao, with assistance from Z. Li and S. Liu, prepared the crystal samples. M. Guo and W. Xiao performed the experiments, with help from F. Wang. M. Guo

completed the theoretical modeling and analysis with assistance of W. Sun, F. Wang, P. Wang and M. Zhong. M. Guo wrote the manuscript with help from S. Liu, F. Wang, and M. Zhong. All authors discussed the results and contributed to the final manuscript.

Competing interests

The authors declare no competing interests.

References

[1] K. Azuma, S. E. Economou, D. Elkouss, P. Hilaire, L. Jiang, H.-K. Lo, and I. Tzitrin, Rev. Mod. Phys. **95**, 045006 (2023)

[2] K. Heshami, D. G. England, P. C. Humphreys, P. J. Bustard, V. M. Acosta, J. Nunn, and B. J. Sussman, Journal of modern optics **63**, 2005 (2016)

[3] N. Sangouard, C. Simon, H. de Riedmatten, and N. Gisin, Rev. Mod. Phys. **83**, 33 (2011)

[4] M. Guo, S. Liu, W. Sun, M. Ren, F. Wang, and M. Zhong, Frontiers of Physics **18**, 21303 (2023)

[5] C. Thiel, T. Böttger, and R. Cone, Journal of Luminescence **131**, 353 (2011)

[6] M. Zhong, M. P. Hedges, R. L. Ahlefeldt, J. G. Bartholomew, S. E. Beavan, S. M. Wittig, J. J. Longdell, and M. J. Sellars, Nature **517**, 177 (2015)

[7] Y. Ma, Y.-Z. Ma, Z.-Q. Zhou, C.-F. Li, and G.-C. Guo, Nature communications **12**, 2381 (2021)

[8] A. Ortu, A. Holzäpfel, J. Etesse, and M. Afzelius, noop npj Quantum Information **8**, 29 (2022)

[9] T. H. Taminiau, J. J. T. Wagenaar, T. van der Sar, F. Jelezko, V. V. Dobrovitski, and R. Hanson, Phys. Rev. Lett. **109**, 137602 (2012)

[10] Z.-Q. Zhou, C. Liu, C.-F. Li, G.-C. Guo, D. Oblak, M. Lei, A. Faraon, M. Mazzera, and H. de Riedmatten, Laser & Photonics Reviews **17**, 2300257 (2023)

[11] D.-C. Liu, P.-Y. Li, T.-X. Zhu, L. Zheng, J.-Y. Huang, Z.-Q. Zhou, C.-F. Li, and G.-C. Guo, Phys. Rev. Lett. **129**, 210501 (2022)

[12] E. Saglamyurek, M. Grimau Puigibert, Q. Zhou, L. Giner, F. Marsili, V. B. Verma, S. Woo Nam, L. Oesterling, D. Nippa, D. Oblak, *et al.*, Nature communications **7**, 11202 (2016)

[13] E. Saglamyurek, J. Jin, V. B. Verma, M. D. Shaw, F. Marsili, S. W. Nam, D. Oblak, and W. Tittel, Nature Photonics **9**, 83 (2015)

[14] I. Craiciu, M. Lei, J. Rochman, J. M. Kindem, J. G. Bartholomew, E. Miyazono, T. Zhong, N. Sinclair, and A. Faraon, Phys. Rev. Appl. **12**, 024062 (2019)

[15] R. Ahlefeldt, N. Manson, and M. Sellars, Journal of Luminescence **133**, 152 (2013), 16th International Conference on Luminescence ICL'11

[16] F. Kimiaee Asadi, N. Lauk, S. Wein, N. Sinclair, C. O'Brien, and C. Simon, Quantum **2**, 93 (2018)

[17] R. Ahlefeldt, M. Zhong, J. Bartholomew, and M. Sellars, Journal of Luminescence **143**, 193 (2013)

[18] R. L. Ahlefeldt, W. D. Hutchison, N. B. Manson, and M. J. Sellars, Phys. Rev. B **88**, 184424 (2013)

[19] R. Ahlefeldt, Evaluation of a stoichiometric rare earth crystal for quantum computing, noop Ph.D. thesis (2013)

[20] M. B. Schulz and C. D. Jeffries, Phys. Rev. **159**, 277 (1967)

[21] S. B. Altner, U. P. Wild, and M. Mitsunaga, Chemical Physics Letters **237**, 406 (1995)

[22] R. L. Ahlefeldt, D. L. McAuslan, J. J. Longdell, N. B. Manson, and M. J. Sellars, Phys. Rev. Lett. **111**, 240501 (2013)

[23] J. J. Longdell, M. J. Sellars, and N. B. Manson, Phys. Rev. Lett. **93**, 130503 (2004)

[24] F. Könz, Y. Sun, C. W. Thiel, R. L. Cone, R. W. Equall, R. L. Hutcheson, and R. M. Macfarlane, Phys. Rev. B **68**, 085109 (2003)

[25] N. Kunkel, J. Bartholomew, S. Welinski, A. Ferrier, A. Ikesue, and P. Goldner, Phys. Rev. B **94**, 184301 (2016)

[26] A. Abragam and B. Bleaney, noop *Electron paramagnetic resonance of transition ions* (OUP Oxford, 2012)

[27] M. Mitsunaga, R. Yano, and N. Uesugi, Phys. Rev. B **45**, 12760 (1992)

[28] S. Probst, G. Zhang, M. Rančić, V. Ranjan, M. Le Dantec, Z. Zhang, B. Albanese, A. Doll, R. B. Liu, J. Morton, T. Chanelière, P. Goldner, D. Vion, D. Esteve, and P. Bertet, Magnetic Resonance **1**, 315 (2020)

[29] F. Wang, M. Ren, W. Sun, M. Guo, M. J. Sellars, R. L. Ahlefeldt, J. G. Bartholomew, J. Yao, S. Liu, and M. Zhong, PRX Quantum **6**, 010302 (2025)

[30] W. B. Mims, Phys. Rev. **168**, 370 (1968)

[31] L. Couture and K. Rajnak, Chemical Physics **85**, 315 (1984)

[32] M. Rančić, M. P. Hedges, R. L. Ahlefeldt, and M. J. Sellars, Nature Physics **14**, 50 (2018)

[33] A. Ruskuc, C. J. Wu, J. Rochman, J. Choi, and A. Faraon, Nature **602**, 408 (2022)

[34] I. Schwartz, J. Scheuer, B. Tratzmiller, S. Müller, Q. Chen, I. Dhand, Z.-Y. Wang, C. Müller, B. Naydenov, F. Jelezko, *et al.*, Science advances **4**, eaat8978 (2018)

[35] J. Choi, H. Zhou, H. S. Knowles, R. Landig, S. Choi, and M. D. Lukin, Phys. Rev. X **10**, 031002 (2020)

[36] J. Freeman, G. Crosby, and K. Lawson, Journal of Molecular Spectroscopy **13**, 399 (1964)

[37] R. Ahlefeldt, W. Hutchison, and M. Sellars, Journal of Luminescence **130**, 1594 (2010)

.

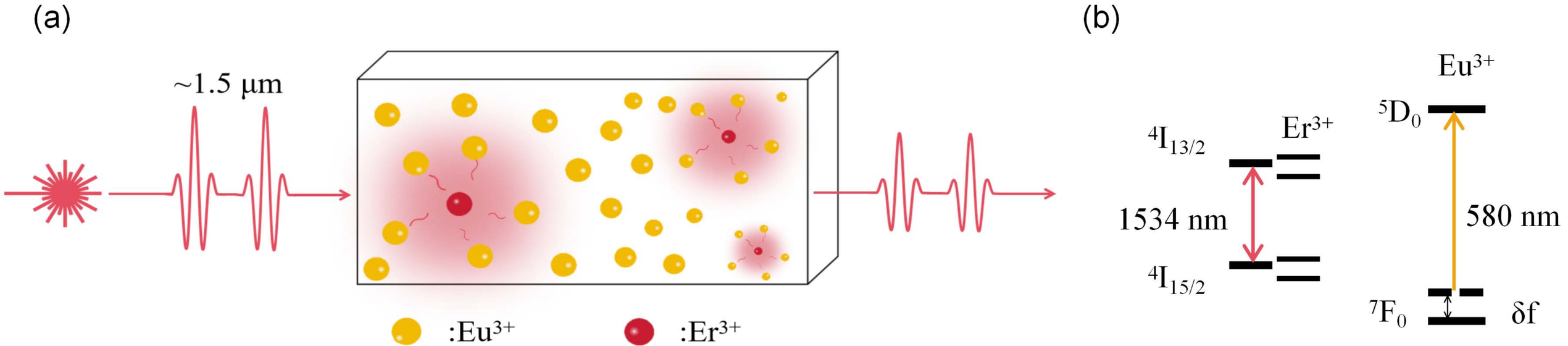
(a)
~1.5 μm
:Eu3+
:Er3+
(b)
Er3+
4I13/2
1534 nm
4I15/2
Eu3+
5D0
580 nm
7F0
δf

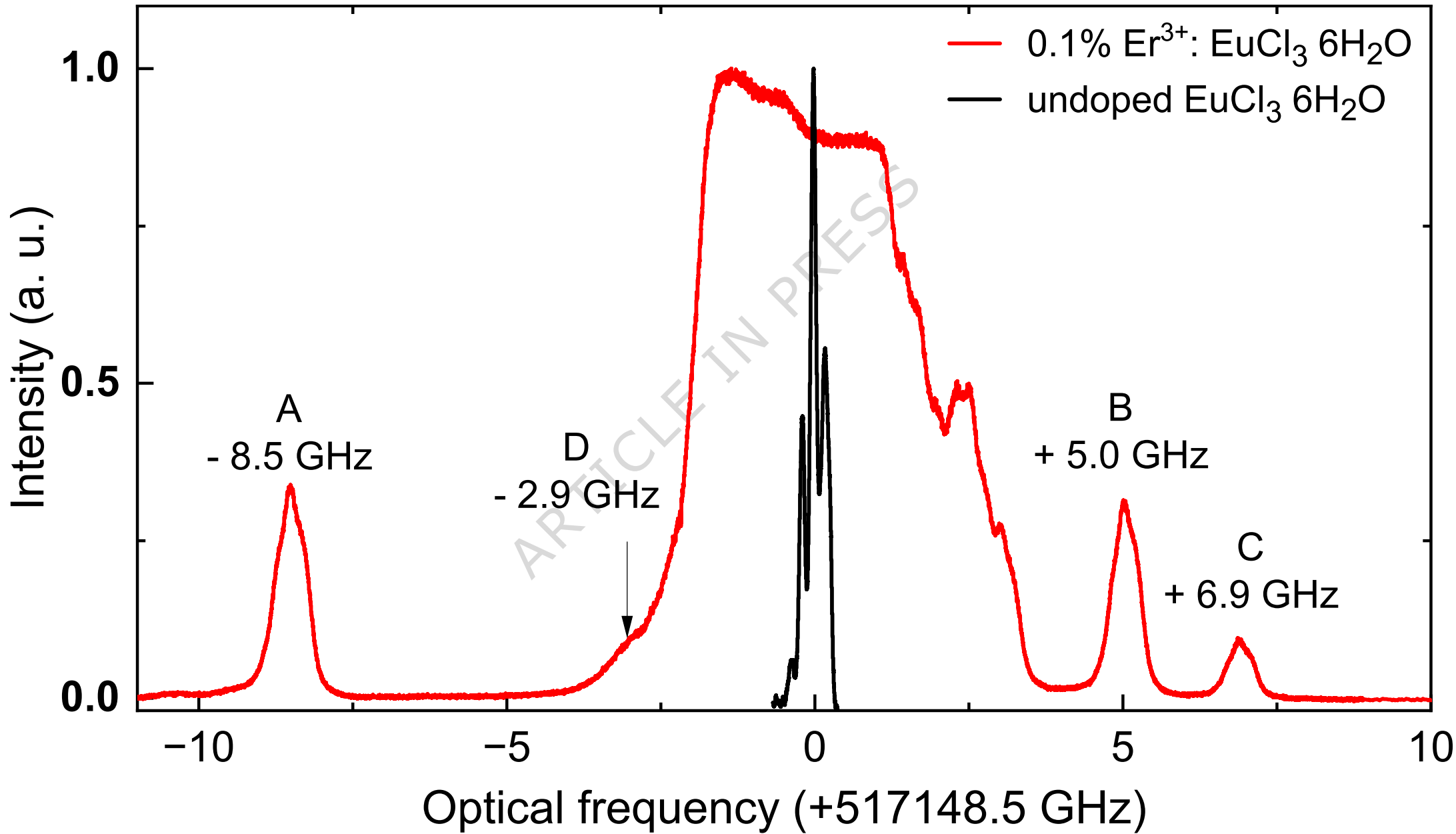

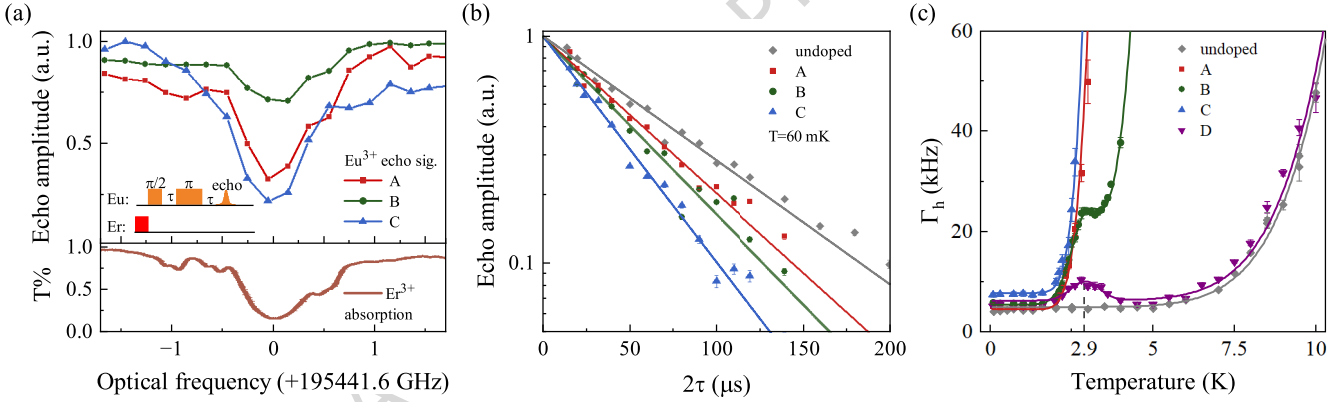

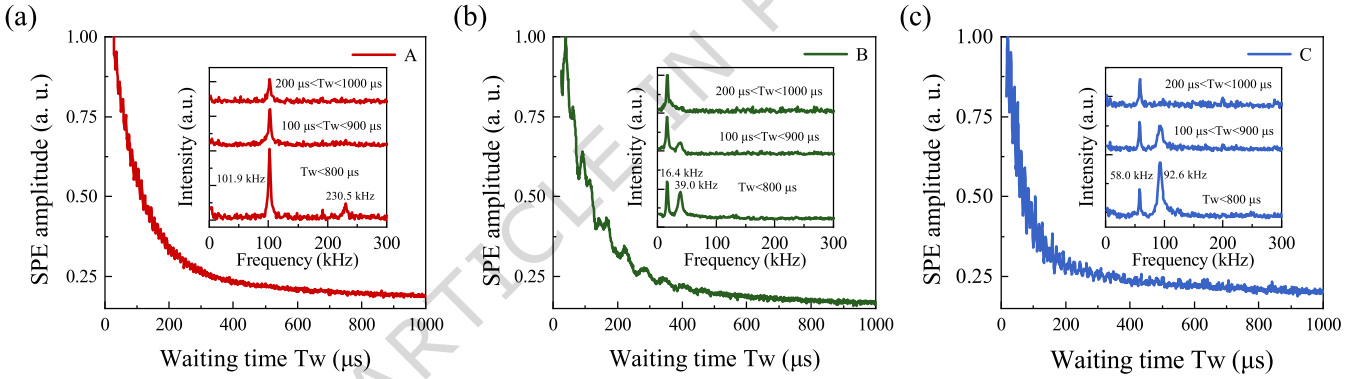

(a)

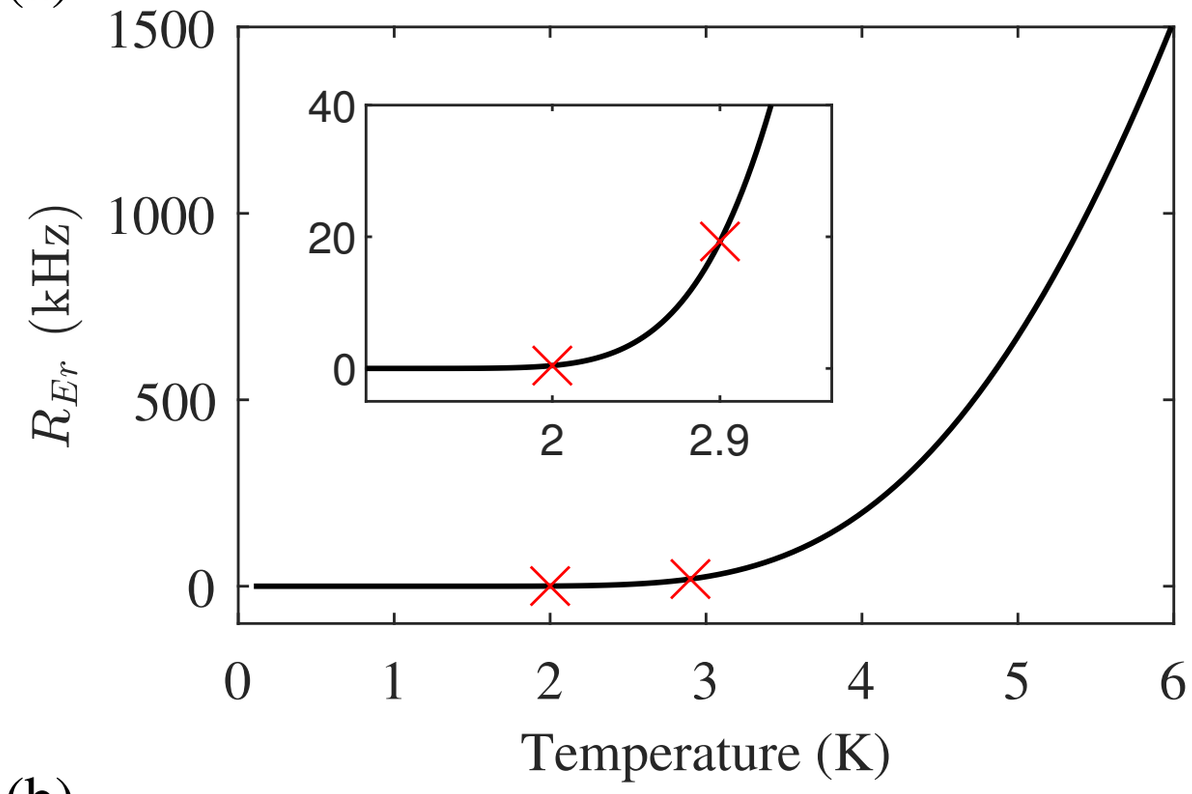

(b)

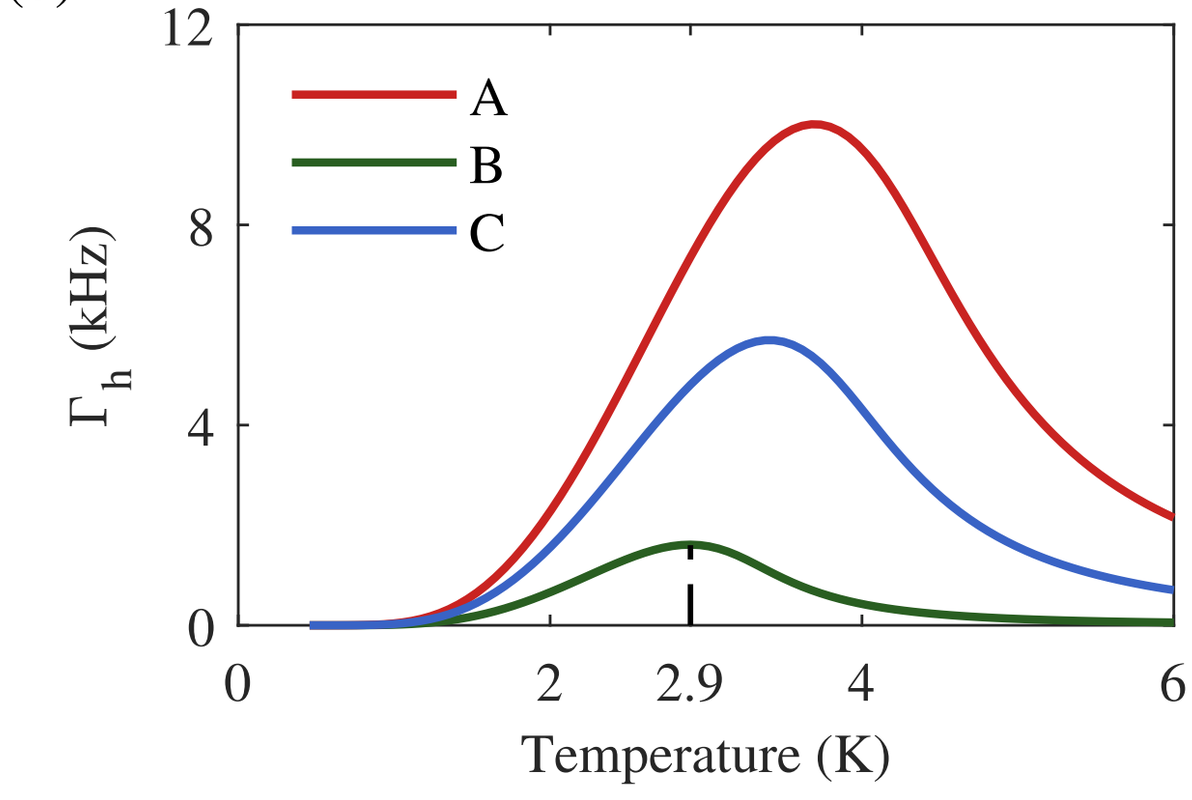

(a)

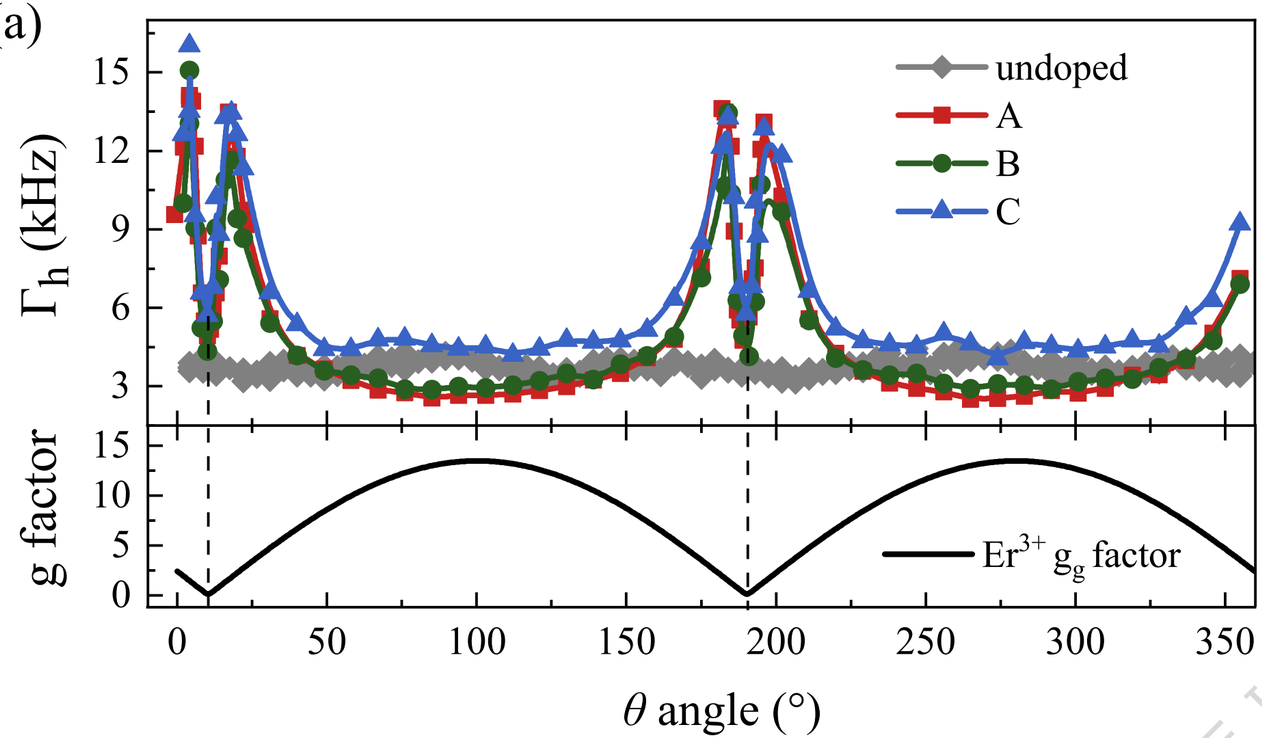

(b)

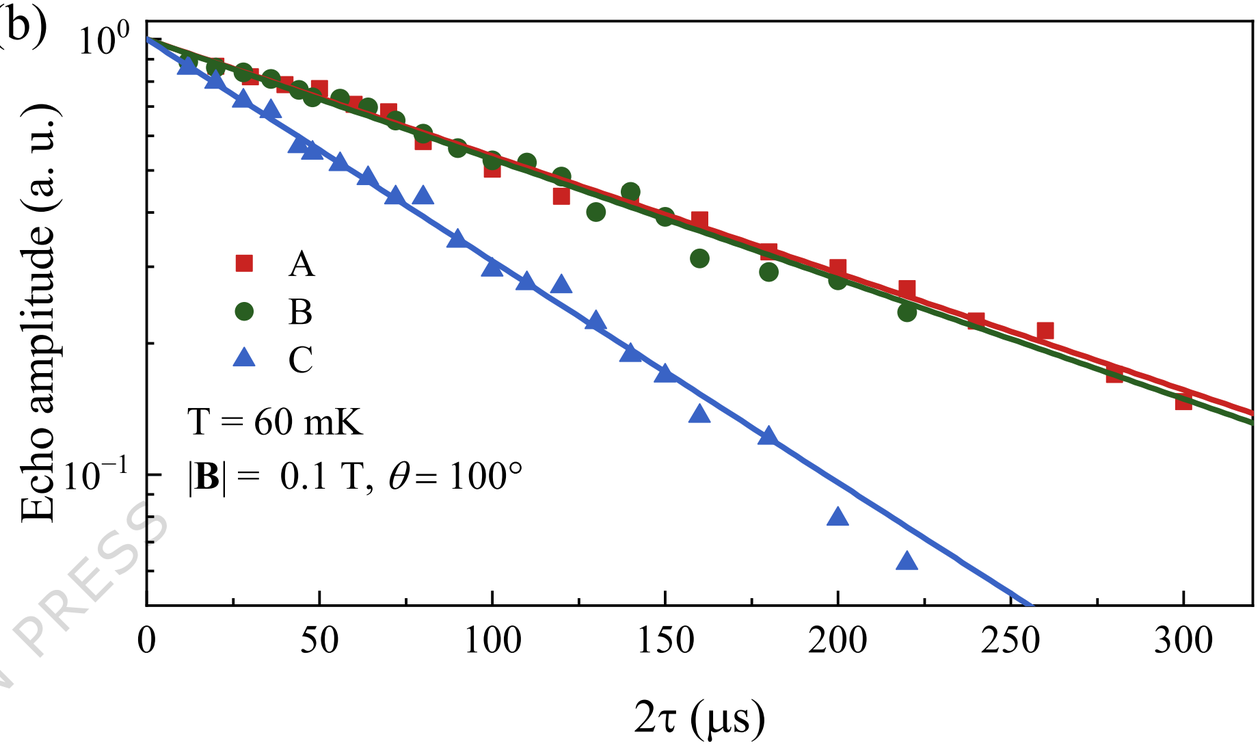

(c)

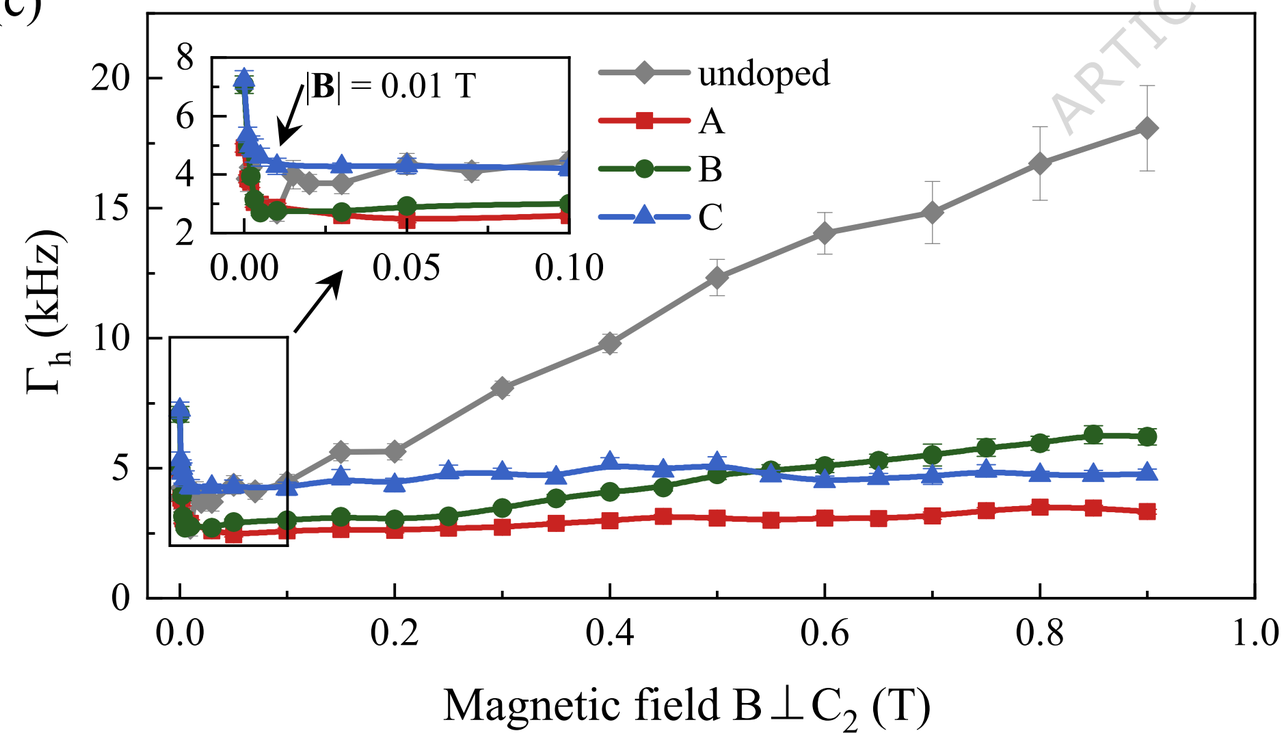

(d)